Efficient representation of long-range interactions in tensor network algorithms

Matthew J. O'Rourke, Zhendong Li, and Garnet Kin-Lic Chan

Phys. Rev. B **98**, 205127 — Published 16 November 2018

DOI: 10.1103/PhysRevB.98.205127

Efficient representation of long-range interactions in tensor network algorithms

Matthew J. O'Rourke, Zhendong Li, and Garnet Kin-Lic Chan
Division of Chemistry and Chemical Engineering,
California Institute of Technology, Pasadena, California 91125, USA

We describe a practical and efficient approach to represent physically realistic long-range interactions in two-dimensional tensor network algorithms via projected entangled-pair operators (PEPOs). We express the long-range interaction as a linear combination of correlation functions of an auxiliary system with only nearest-neighbor interactions. To obtain a smooth and radially isotropic interaction across all length scales, we map the physical lattice to an auxiliary lattice of expanded size. Our construction yields a long-range PEPO as a sum of ancillary PEPOs, each of small, constant bond dimension. This representation enables efficient numerical simulations with long-range interactions using projected entangled pair states.

I. INTRODUCTION

The accurate description of strongly correlated quantum many-body systems is a major challenge in contemporary physics. Nonetheless, some of the most intriguing macroscopic quantum phenomena, such as high-temperature superconductivity and the fractional quantum Hall effect, arise from strong quantum correlations. In recent years, tensor network states (TNS) [1–6], including matrix product states (MPS) [7–10] and projected entangled-pair states (PEPS) [11–14], have emerged as promising classes of variational states to numerically approximate the low energy physics of correlated quantum systems with area or near-area law physics. Their power stems from systematically improvable accuracy through increasing the tensor bond dimension D [15], and the $O(A)$ linear complexity of the associated algorithms with respect to the system size A (under assumption of contractibility of the underlying tensor network, as is common in many physical applications, using approximate contraction methods [11, 12, 16–20].)

One promising application of TNS is to accurate calculations of electronic structure of realistic materials. While the electronic structure Hamiltonian can be represented in multiple ways [21–24], the simplest – and the one of interest in this work – is a real-space grid formulation [25–29],

$$\begin{aligned}\hat{H} &= -t \sum_{<i,j>} (a^\dagger_{i\sigma} a_{j\sigma} + h.c.) + \sum_i v^{ne}_i n_i + \hat{V}^{ee}, \\ \hat{V}^{ee} &= \sum_i v^{ee}_{ii} n_{i\alpha} n_{i\beta} + \sum_{i<j} v^{ee}_{ij} n_i n_j, \end{aligned} \tag{1}$$

where i, j label lattice sites, $\sigma \in \{\alpha, \beta\}$ labels spin, t is the kinetic energy matrix element, and $a^\dagger$, a, and n are fermion creation, annihilation, and number operators, respectively. As the spacing between grid points (h) goes to zero, the parameters scale as $t \propto h^{-2}$ and $v^{ee}_{ij} \propto h^{-1}$; these become exact representations of $-\frac{1}{2}\nabla^2$ and the continuum Coulomb potential $1/r_{ij}$ with $r_{ij} \triangleq |\mathbf{r}_i - \mathbf{r}_j|$ [26, 28]. This simple form of the electronic structure Hamiltonian is especially suited to TNS algorithms as the Coulomb interaction is a pairwise operator as opposed to a general quartic operator when using a non-local basis, and Eq. (1) can be viewed as an extended Hubbard model with long-range terms. Ground states of such grid Hamiltonians have been computed in 1D using MPS and the density matrix renormalization group (DMRG), yielding near exact electronic structure benchmarks for small lattice spacings [1, 2, 25]. In principle, this success in 1D should be extensible to 2D and 3D by using PEPS instead of MPS, and would then provide a route to simulate arbitrarily complex electronic structure problems with arbitrarily improvable accuracy.

However, current state-of-the-art PEPS applications to physical problems have not yet advanced beyond local lattice models in 2D [18, 30–34]. There are two principal complications. The first is that long-range interactions can in principle lead to increased entanglement, and even volume-law entanglement, that would be difficult or impossible to capture with a PEPS with a finite bond dimension. Fortunately, in applications of the density matrix renormalization group using the Coulomb interaction (for example, to electronic structure) it is seen that the increase in entanglement is modest and volume law entanglement is not observed [23, 25, 35–38]. The second complication is simply the increased cost of all operations when long-range interactions are considered, even for a fixed bond dimension. To see the basic challenge, consider the evaluation of the energy expectation value: for a Hamiltonian with localized interactions, the number of terms in a standard term-by-term calculation scales linearly with the size of the system, $O(A)$. However, for a Hamiltonian with long-range interactions, the number of terms scales like $O(A^2)$, which is prohibitively expensive in two (or higher) dimensions, as we take the continuum limit. Alternatively, one might try to use an exact tensor network operator, or projected entangled pair operator (PEPO), to represent the long-range interaction [39], avoiding the explicit term-by-term evaluation. However, the exact PEPO representation for arbitrary long-range interactions in 2D has a bond dimension that scales as $O(A^{1/4})$, causing the overall cost to compute expectation values to scale as $O(A^2)$ [40].

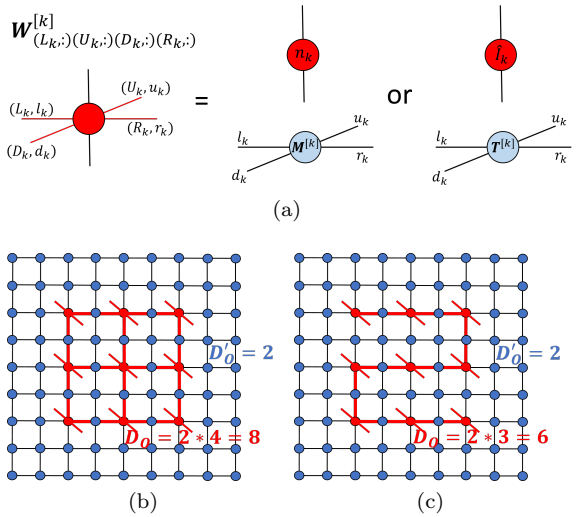

FIG. 1. (a) The construction of the nonzero parts of the CF-PEPO tensor $\mathbf{W}^{[k]}$ via the coupling of the finite state machine (FSM) tensor (red) with the Ising correlation function tensors (blue). Note that here the physical indices of $\mathbf{W}^{[k]}$ are explicitly shown, whereas they are suppressed in Eq. (3). (b)-(c) Two possible constructions of the long-range PEPO for a 3x3 physical system with 1 fictitious Ising site (blue) in between adjacent physical sites (red) and a 2 site buffer to help mitigate boundary effects in the encoding of the potential. Black bonds are $D'_O = 2$ and red bonds are $D_O = 8$ (b) and 6 (c).

In 1D, the increased computational cost of long-range interactions can be eliminated if they are smooth and decaying. In this case one can approximate the exact matrix product operator (MPO) by a compressed MPO of constant bond dimension D that generates a sum of exponential interactions, and smoothly decaying interactions can be approximated well by such sums [39, 41, 42]. Exponential interactions in MPOs arise naturally from the matrix product structure, which also gives rise to the exponential decay of two-point correlation functions in MPS. Extending the correlation function analogy to 2D leads to an efficient representation of long range interactions in 2D when their form exactly coincides with the correlation function of a 2D lattice model. This was demonstrated in Ref. [39], which constructed a compact pair interaction PEPO whose interaction potential was given by the critical 2D Ising correlation function.

Building on these ideas, in this work we describe how general long-range interactions in two dimensions, including the Coulomb interaction, can be efficiently encoded as a sum of low rank correlation function valued PEPOs. Although superficially similar to the problem of approximating a smooth interaction in 1D by a sum of exponentials, additional complications arise in two dimensions because physical interactions possess different analytic properties from two-point correlation functions on the same lattice. For example, the Coulomb interaction is radially isotropic at all distances, while the two-point lattice correlation functions are isotropic only at large distances due to the lattice discretization. We show how to overcome these and other difficulties by introducing an expanded auxiliary lattice, and demonstrate the effectiveness of the representation in a ground-state finite PEPS simulation of a 2D spin model with Coulombic Heisenberg interactions. Although we specifically treat only the Coulomb interaction and two dimensions in our numerical examples, our arguments naturally extend to representing smooth and radially isotropic interactions in any dimension.

II. CORRELATION FUNCTION VALUED PEPOS

We first define correlation function valued PEPOs (CF-PEPOs), which are central to this work. As motivation, we recall the construction of MPOs for smooth interactions approximated by sums of exponentials. This is usually done in the language of finite state machines (FSM), where the MPO is viewed as an operator valued MPS, and the incoming and outgoing bonds of each MPO tensor are interpreted as machine states [41, 42]. An FSM can encode an exponentially decaying interaction strength $e^{-\lambda r_{ij}}$ via a single non-zero element in each MPO tensor with value $e^{-\lambda}$, that gets multiplied along the lattice as long as the FSM stays in a specified state. The pairwise operator $\sum_{i<j} e^{-\lambda r_{ij}} n_i n_j$ can then be represented by an MPO with bond dimension 3, with the two additional states in the FSM acting to combine the exponential scalar values with the operators $n_i n_j$. The construction can be extended to the general 1D interaction $\sum_{i<j} V(r_{ij}) n_i n_j \approx \sum_{i<j} \sum_{t=1}^{N_t} c_t e^{-\lambda_t r_{ij}} n_i n_j$ by introducing additional states for each of the N_t exponential decays, for a total MPO bond dimension of $N_t + 2$ (or alternatively, N_t MPOs of bond dimension 3). However, while this representation is natural in 1D, its direct extension to 2D is not. This is because multiplying the element $e^{-\lambda}$ along any single FSM path between two sites i and j creates an exponentially decaying strength as a function of the Manhattan distance $|x| + |y|$, not the desired Euclidean distance $(x^2 + y^2)^{1/2}$, as the elements are multiplied out along the grid lines [40].

A different starting point, that is more natural in higher dimensions, is to consider scalar interaction strengths generated by the two-point correlation function $\langle o(\mathbf{r}_i) o(\mathbf{r}_j) \rangle_\beta$ of a classical model at inverse temperature β. We term the PEPO for the operator $\sum_{i<j} \langle o(\mathbf{r}_i) o(\mathbf{r}_j) \rangle_\beta n_i n_j$, a correlation function valued PEPO (CF-PEPO). Using a classical model with local interactions yields a CF-PEPO with low bond dimension, as noted in Ref. [39]. As a concrete example, consider the spin-spin correlation function $\langle \sigma_i \sigma_j \rangle$ of the 2D Ising model, which has the Hamiltonian $H = -\sum_{\langle m,n \rangle} \sigma_m \sigma_n$, $\sigma \in \{+1, -1\}$. For two given points on the lattice i and j, this correlation can be exactly represented by the Ising

PEPS with $D = 2$ [13, 43], viz.,

$$\langle \sigma_i \sigma_j \rangle_\beta = \frac{1}{Z} \mathrm{Tr} \left(\prod_{k \neq i,j} T^{[k]}_{l_k u_k d_k r_k} M^{[i]}_{l_i u_i d_i r_i} M^{[j]}_{l_j u_j d_j r_j} \right). \tag{2}$$

Here $Z = \mathrm{Tr} \prod_k \mathbf{T}^{[k]}$ is the partition function and the tensors $\mathbf{T}$ and $\mathbf{M}$ are the local tensors of the PEPS off and on the correlation function sites, respectively. These tensors are obtained from the eigenvalue decomposition $X = U\lambda U^{\mathrm{T}}$ of the familiar 2×2 Ising model transfer matrix $X_{ij} = \exp((-1)^{\delta_{ij}+1} J\beta)$, which encodes the local terms of the partition function for a pair of nearest neighbor spins [44]. In tensor network language, these X matrices would be placed on each bond of the square lattice. In order to create a local tensor network description of the system, we define the "square root" of this transfer operator as $P = U\sqrt{\lambda}U^{\mathrm{T}}$, and define the local tensors as $T_{ludr} = \sum_a P_{la} P_{ua} P_{ad} P_{ar}$ and $M_{ludr} = \sum_{ab} P_{la} P_{ua} P_{da} \sigma^z_{ab} P_{br}$, where σ^z is the standard Pauli matrix.

To obtain the Ising CF-PEPO, we combine the tensors $\mathbf{T}^{[k]}$, $\mathbf{M}^{[k]}$ of the Ising PEPS at each site with (translationally invariant) tensors $\mathbf{Y}^{[k]}$ of a PEPO for the interaction $\sum_{i<j} n_i n_j$. As demonstrated in a general fashion in [40] based on work in [41], the $\mathbf{Y}^{[k]}$ tensors can be obtained by a FSM construction in 2D, where each element of the tensor $Y_{L,U,D,R}$ at a given site corresponds to a specific local state of the FSM and returns a specific local operator $\{0, \hat{I}, n\}$. The Ising CF-PEPO tensors are then formed by a selective direct product between $\mathbf{Y}^{[k]}$, $\mathbf{T}^{[k]}$, and $\mathbf{M}^{[k]}$,

$$\begin{aligned}
\sum_{i<j} \langle \sigma_i \sigma_j \rangle_\beta n_i n_j &= \mathrm{Tr} \left(\prod_k W^{[k]}_{(L_k,l_k)(U_k,u_k)(D_k,d_k)(R_k,r_k)} \right), \\
\mathbf{W}^{[k]}_{(L_k,:)(U_k,:)(D_k,:)(R_k,:)} &= Y^{[k]}_{L_k,U_k,D_k,R_k} \otimes \mathbf{T}^{[k]} \text{ if } Y = \hat{I}_k, \\
\mathbf{W}^{[k]}_{(L_k,:)(U_k,:)(D_k,:)(R_k,:)} &= Y^{[k]}_{L_k,U_k,D_k,R_k} \otimes \mathbf{M}^{[k]} \text{ if } Y = n_k, \\
\mathbf{W}^{[k]}_{(L_k,:)(U_k,:)(D_k,:)(R_k,:)} &= 0 \text{ if } Y = 0.
\end{aligned} \tag{3}$$

Here $\mathbf{W}^{[k]}$ (Fig. 1(a)) is the operator valued tensor in the Ising CF-PEPO and (L_k, l_k) is a composite index of the bond L_k for the 2D FSM and the bond l_k of the Ising PEPS. Note that the selective direct product can be formed unambiguously due to the $1:1$ correspondence between possible states of $\mathbf{Y}^{[k]}$ and the Ising PEPS tensors $\mathbf{M}^{[k]}$ and $\mathbf{T}^{[k]}$.

Since the FSM tensors $\mathbf{Y}^{[k]}$ only need to encode the two operators $n_i n_j$ and contain no information about the distance between them, there is some flexibility in the possible topologies of the FSM (see Fig. 1). The snake geometry in (c) has a significantly reduced computational complexity compared to the original FSM from [40] shown in (b), and it also imposes an ordering that allows for a simple way to include fermionic statistics (via Jordan-Wigner strings) at the operator level, eliminating the need for swap gates in fermionic PEPS [45]. The full specifications for constructing the tensors $\mathbf{Y}^{[k]}$ according to both FSM geometries are given in Appendix A. As an important note, both of these constructions are compatible with existing iPEPS [46] algorithms.

III. CF-PEPOS AND THE AUXILIARY LATTICE

Using the above arguments, we might now consider approximating the form of a physical, smooth, and isotropic interaction $V(r_{ij})$ by a sum of N_t lattice correlation functions at different temperatures, $V(r_{ij}) \approx V_{\mathrm{fit}}(r_{ij}) = \sum_{t=1}^{N_t} c_t f_{\beta_t}(r_{ij})$ [$f_{\beta_t}(r_{ij}) \triangleq \langle o(\mathbf{r}_i) o(\mathbf{r}_j) \rangle_{\beta_t}$], giving the interaction operator as a sum of CF-PEPOs. In Fig. 2(a) we show the maximal absolute error in a direct fit of $1/r_{ij}$ using Ising correlation functions on an LxL lattice. For large r_{ij}, the maximal error (at a given radius) can be seen to converge rapidly, with a fitted convergence rate of $\sim O(r_{ij}^{-2.7})$ (Fig. 2(a)), showing we can easily capture the long distance behavior of the Coulomb potential that is sampled at large system sizes. However, for small r_{ij}, the maximal errors are much larger, and the expansion does *not* converge even with very many terms, as seen in Fig. 2(b). This is because the lattice discretization of the correlation functions prevents radial isotropy in the basis $\{f_{\beta_t}\}$ at short lattice distances. In addition, for finite lattices, boundary effects also cause errors in the isotropy and translational invariance.

The short distance anisotropy error can be remedied by representing the isotropic physical interaction by correlation functions generated on an *expanded auxiliary lattice* with additional "fictitious" sites. The physical distance r_{ij} (on the original lattice) maps to the expanded distance $R_{ij} = (N_f + 1) r_{ij}$ on the auxiliary lattice (N_f denotes the number of fictitious sites added to the sides of one unit square on the original lattice). This gives us a rescaled potential that is easier to fit at small r_{ij},

$$\tilde{V}^{[N_f]}_{\mathrm{fit}}(r_{ij}) \triangleq (N_f + 1) V_{\mathrm{fit}}(R_{ij}) = (N_f + 1) \sum_{t=1}^{N_t} c_t f_{\beta_t}(R_{ij}), \tag{4}$$

where the specific rescaling in Eq. (4) has been shown for the Coulomb potential. Choosing a sufficiently large expansion factor N_f ensures that the fitting basis becomes isotropic up to an error ϵ, and the radial fit can then be performed to increasing accuracy with increasing N_t up to a similar ϵ. Further, choosing a suitably large side length of the auxiliary lattice buffering the physical region also removes the boundary effects in a finite lattice simulation.

In Figs. 2(b)-(c) we show the behavior of the maximal error in fitting $\tilde{V}^{[N_f]}_{\mathrm{fit}}(r_{ij})$ to $1/r_{ij}$ for several values of r_{ij}, as a function of both the number of fictitious sites N_f and

fitting terms N_t. They demonstrate that for $N_f = 10$ and a modest $N_t = 8$, we are able to obtain a maximum error of 10^{-3} with $\tilde{V}_{\text{fit}}^{[10]}(r_{ij})$. In Fig. 2(c), note that the $r_{ij} = 1$ curve (i.e. the maximal error curve) converges as $\sim (N_f+1)O(N_f^{-2.7}) \propto N_f^{-1.7}$ due to the rescaling factor in Eq. (4). Thus by further increasing N_f the error can be continually decreased.

Up to this point in this section, we have implicitly considered r_{ij} only on the unit lattice, i.e., $r_{ij} \triangleq |(x,y)_i - (x,y)_j|; x,y \in \mathbb{Z}$, which is to say that the lattice spacing $h = 1$. In addition to the above discussion of increasing N_f to reduce the fitting error for a fixed spacing $h = 1$, an alternative (but equivalent) viewpoint is that N_f can be increased to maintain a given maximal error in the potential as $h \to 0$. Precisely, the maximal error in the new potential will occur at the new shortest physical distance, $V(h) = h^{-1}\tilde{V}_{\text{fit}}^{[N_f]}(1)$. The error at this point $\epsilon(V(h))$ scales as $\epsilon \propto h^{-1}N_f^{-1.7}$, which reveals that N_f must increase as $N_f \propto h^{-1/1.7} = h^{-0.59}$ in order to maintain the level of error originally incurred at the point $\tilde{V}_{\text{fit}}^{[N_f]}(1)$ (for $h = 1$).

In summary, the full CF-PEPO is obtained by coupling the FSM of the operators (either in the snake form, or the full 2D FSM) to the Ising CF-PEPS on an expanded lattice as specified by Eq. (4), and as shown in Fig. 1(b)-(c). The total error of the fit is controlled by the expansion parameter N_f and the number of terms N_t. For the Coulomb interaction and a desired accuracy, N_t is only weakly dependent on the physical lattice discretization and system size. This is similar to what is observed in MPO fits in one dimension [25, 39, 41, 42] as well as analytical work on exponential fits of the Coulomb operator in 2D [47].

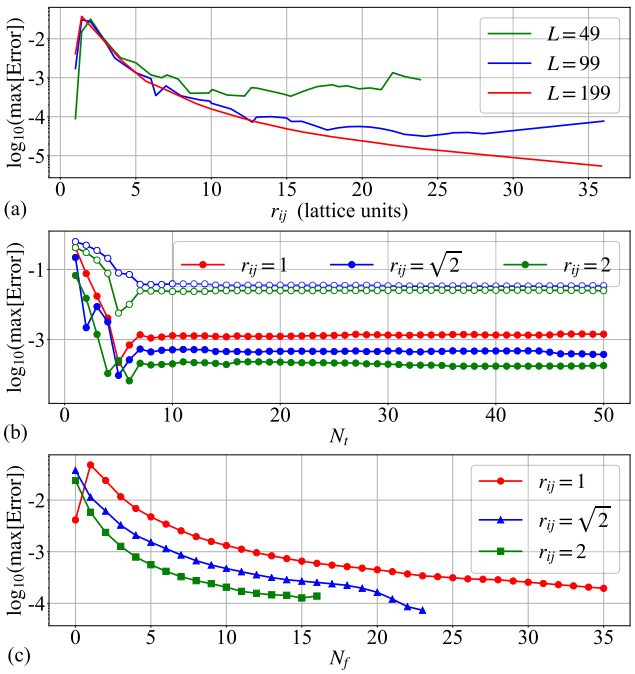

FIG. 2. Convergence properties of Coulomb fitting. For all plots $r_{ij} = 0$ is the central point on the lattice. (a) The upper envelope of $|V_{\text{fit}}(r_{ij}) - 1/r_{ij}|$ obtained with $N_t = 12$, $r_{ij} = R_{ij}$, a least squares weight function of $r_{ij}^{1.5}$, and Ising model lattices with different side lengths L. The fits were performed on a disc with radius equal to the maximum r_{ij} displayed for a given curve. (b) and (c): The maximum fitting error $\left|\tilde{V}_{\text{fit}}^{[N_f]} - 1/r_{ij}\right|$ at selected values of r_{ij} as functions of N_t (b) and N_f (c). In (b), the open circles correspond to $N_f = 0$ and the closed circles to $N_f = 10$. In (c), $N_t = 12$. The fits in (b) and (c) were performed on discs of radius $r_{ij} = 36$ with $L = 199$ and a weight function of $r_{ij}^{1.5}$.

IV. COMPUTATIONAL COST

We now consider the evaluation of a finite PEPS expectation value for a PEPS of bond dimension D_S and an Ising CF-PEPO of bond dimension D_O. To define the computational cost, we must choose an approximate contraction scheme. Here we use a simple generalization of the "optimized" contraction scheme proposed in Ref. [48] to include a PEPO. Using the full 2D FSM (Fig. 1(b)), the CF-PEPO has bond dimension $D_O = 8$ for the bonds emanating from the physical sites and $D'_O = 2$ for bonds that only connect fictitious sites, and the leading contraction cost can be derived to be $N_t[O(A\chi^3 D_O^3) + O(AN_f\chi^3 D_O'^2 D_O) + O(AN_f^2\chi^3 D_O'^3) + O(A\chi^3 D_S^3) + O(AN_f\chi^3 D_O'^2 D_S)]$, where χ is the maximum bond dimension appearing in the approximate contraction scheme and can be taken as $\chi \sim D_S^2 D_O$. For the snake FSM construction (Fig. 1(c)) $D_O = 6$ instead of 8, and the physical PEPO tensors only have two large bond dimensions instead of four. This reduces the overall scaling to $N_t[O(A\chi^3 D_O'^2 D_O) + O(AN_f\chi^3 D_O'^2 D_O) + O(AN_f^2\chi^3 D_O'^3) + O(A\chi^3 D_S^3) + O(AN_f\chi^3 D_O'^2 D_S)]$.

In both cases, the cost is linear in the system area A as we originally desired. However, it is instructive to compare these costs to an implementation without a PEPO. In a naive implementation of the exact term-by-term contraction of each $n_i n_j$ operator in the Coulomb potential, a single term would involve a contraction of cost $O(A\chi^3 D_S^3)$ with $\chi \sim D_S^2$, and there would be $O(A^2)$ such terms, giving an $O(A^3)$ cost. Assuming a reasonably large value for D_S, this cost can be compared to the analogous term in the (snake) PEPO contraction cost, which gives an approximate crossover when $A^2 \sim N_t D_O^3$, which for $N_t = 10$, $D_O = 6$, corresponds to $A \sim 50$. In a more sophisticated exact implementation, we could rewrite $\sum_{ij} V_{ij} n_i n_j$ as $\sum_i n_i \hat{O}_i$, with $\hat{O}_i = \sum_j V_{ij} n_j$. Each $\hat{O}_i$ can be represented as a snake-like MPO with bond dimension $D = 3$, and the cost of contracting a single $\hat{O}_i$ expectation value is then $O(A\chi^3 D_S^3)$ with $\chi \sim DD_S^2$, with $O(A)$ such terms. The crossover with our (snake) PEPO representation then occurs when $A \sim 8N_t$,

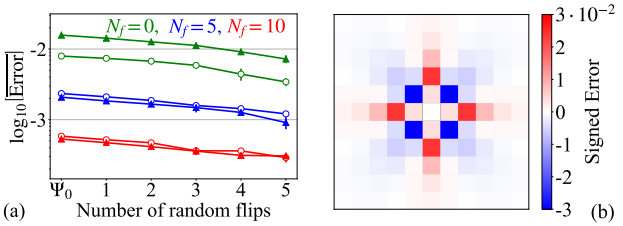

FIG. 3. (a) Average accuracy of energy per site expectation values for 6×6 FM and AFM trial PEPS with $D_S = 1$. The solid triangular markers show FM states while the open circles show AFM states. Ψ_0 is a true FM or AFM state, while the "x flip" regions are Ψ_0 perturbed by x random spin flips. The average error is taken over 5 PEPS for each x and each N_f. (b) The signed error $1/r_{ij} - \tilde{V}^{[0]}_{\text{fit}}(r_{ij})$, where $r_{ij} = 0$ is the white square in the center, each adjacent square is $r_{ij} = 1$, etc. For (a)-(b) the fitted potentials are obtained from Eq. (4) with $N_t = 12$.

which for $N_t = 10$ corresponds to $A < 100$. Thus in either comparison, a crossover between our PEPO representation and other implementations of the long-range operator is achievable already at modest lattice sizes.

V. RESULTS

To numerically test our PEPO's faithful discretized representation of long range interactions, we have explicitly constructed a long-range S=1/2 Heisenberg Hamiltonian on 4×4, 6×6, and 8×8 square lattices,

$$\hat{H} = \sum_{i<j} \frac{\vec{S}_i \cdot \vec{S}_j}{r_{ij}}, \tag{5}$$

in which every pair of spins has an interaction strength of Coulomb form. To represent this operator, we first used the fitting scheme described in Eq. (4) with $N_t = 12$. Figure 3(a) shows the accuracy of the energy per site expectation value (e_0) for 6×6 trial ferromagnetic (FM) and anti-ferromagnetic (AFM) PEPS with $D_S = 1$. The FM and AFM states show similar levels of error for a given value of N_f, indicating that the fitted operator can obtain similar levels of error even for states which have different structures of the *signed* error.

We next performed a simple gradient-based variational optimization for the ground state PEPS with $D_S = 1, 2$ [49, 50]. Note that our goal here is not to demonstrate fully converged physics with respect to the PEPS bond dimension, which will be discussed in future studies, but rather to show that our PEPO leads to a stable optimization procedure. Here we refined the fit for each lattice size to ensure that the maximum PEPO fitting error was limited to $\sim 4.5 \cdot 10^{-4}$ with only $N_f = 4$, $N_t = 12$. Fig. 4 shows the initial convergence behavior of the energy optimization using the PEPO compared to the same optimization using the more expensive sum over terms formalism. We observe that the trajectories are similar

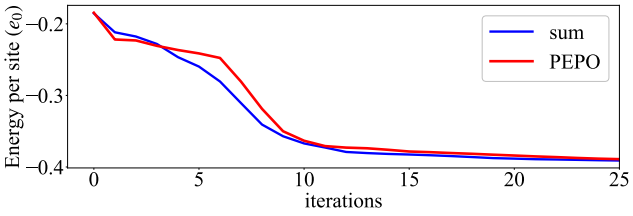

	χ	sum e_0	PEPO e_0	$\langle\psi_0^{[P]}\|\psi_0^{[s]}\rangle$
4×4, $D_S = 1$	40	-0.184314	-0.184425	0.999244
4×4, $D_S = 2$	100	-0.408209	-0.408492	0.999070
4×4, exact	–	0.424577	–	–
8×8, $D_S = 1$	40	-0.193983	-0.193861	0.994549
8×8, $D_S = 2$	120	-0.414653	-0.414422	0.989271
8×8, exact	–	-0.431648	–	–

FIG. 4. *Top*: The trajectories over the first 25 iterations of the energy optimization for the 4×4 $D_S = 2$ system using the PEPO and the explicit sum over all $O(A^2)$ terms in (5). The long tails of the trajectories are excluded for clarity. *Bottom*: Ground state energies per site e_0 for the Hamiltonian (5) with various system sizes and bond dimensions. The fifth column is the overlap of the normalized ground states obtained with the two different methods. In all cases $N_f = 4$ and $N_t = 12$. The "exact" rows are the results of converged DMRG calculations.

and the use of the PEPO does not change the stability of the gradient optimization, although it does require a larger value of χ. The small-D_S converged energies and normalized wavefunction overlaps are given in Fig. 4. In all cases, the CF-PEPO nicely reproduces the explicit sum-over-terms algorithm, as the maximum fitting error is faithfully reflected in the accuracy of e_0. It is also interesting to see that the error of the ground-state energy using $D_S = 2$ is $\sim 3\%$ for both the 4×4 and 8×8 lattice, suggesting that the entanglement does not grow significantly with system size despite the long-range interaction, which is a similar observation to other simulations of physical Coulombic systems.

Conclusions. — In summary, we have detailed the efficient construction of a PEPO capable of encoding long-range interactions in 2D TNS that maintains the strengths of tensor network algorithms: systematically improvable accuracy and linear computational complexity in the system size. Despite an increased cost prefactor compared to local simulations, this approach allows for the possibility of practically including long-range interactions in numerical studies of physically realistic systems that have an entanglement structure consistent with PEPS. The crossover between our approach and other more naive implementations of long-range interactions can be achieved at modest system sizes. In the context of *ab initio* electronic structure calculations, while there remain many issues to explore, in particular associated with the continuum limit of relevance to such applications, this advance presents a first step towards these calculations using higher dimensional tensor networks.

Primary support for this work was from MURI

FA9550-18-1-0095, which supported MJO. Additional support was from the US National Science Foundation via grant CHE-1665333 for ZL. GKC acknowledges support from the Simons Foundation.

[1] S. R. White, Physical review letters **69**, 2863 (1992).
[2] S. R. White, Physical Review B **48**, 10345 (1993).
[3] G. Vidal, Physical review letters **99**, 220405 (2007).
[4] H. J. Changlani, J. M. Kinder, C. J. Umrigar, and G. K.-L. Chan, Physical Review B **80**, 245116 (2009).
[5] F. Mezzacapo, N. Schuch, M. Boninsegni, and J. I. Cirac, New Journal of Physics **11**, 083026 (2009).
[6] G. Carleo and M. Troyer, Science **355**, 602 (2017).
[7] S. Östlund and S. Rommer, Physical review letters **75**, 3537 (1995).
[8] M. Fannes, B. Nachtergaele, and R. F. Werner, Communications in mathematical physics **144**, 443 (1992).
[9] M. Fannes, B. Nachtergaele, and R. Werner, Journal of functional analysis **120**, 511 (1994).
[10] U. Schollwöck, Annals of Physics **326**, 96 (2011).
[11] T. Nishino and K. Okunishi, Journal of the Physical Society of Japan **65**, 891 (1996).
[12] F. Verstraete and J. I. Cirac, arXiv preprint cond-mat/0407066 (2004).
[13] F. Verstraete, M. M. Wolf, D. Perez-Garcia, and J. I. Cirac, Physical review letters **96**, 220601 (2006).
[14] R. Orús, Annals of Physics **349**, 117 (2014).
[15] P. Corboz, Physical Review B **93**, 045116 (2016).
[16] V. Murg, F. Verstraete, and J. I. Cirac, Physical Review A **75**, 033605 (2007).
[17] R. Orús and G. Vidal, Physical Review B **80**, 094403 (2009).
[18] P. Corboz, T. M. Rice, and M. Troyer, Phys. Rev. Lett. **113**, 046402 (2014).
[19] M. Levin and C. P. Nave, Physical review letters **99**, 120601 (2007).
[20] G. Evenbly and G. Vidal, Physical review letters **115**, 180405 (2015).
[21] R. M. Martin, *Electronic structure: basic theory and practical methods* (Cambridge university press, 2004).
[22] A. Szabo and N. S. Ostlund, *Modern Quantum Chemistry: Intro to Advanced Electronic Structure Theory* (Dover publications, 1996).
[23] S. R. White and R. L. Martin, The Journal of chemical physics **110**, 4127 (1999).
[24] G. K.-L. Chan, A. Keselman, N. Nakatani, Z. Li, and S. R. White, The Journal of chemical physics **145**, 014102 (2016).
[25] E. M. Stoudenmire, L. O. Wagner, S. R. White, and K. Burke, Physical review letters **109**, 056402 (2012).
[26] L. O. Wagner, E. Stoudenmire, K. Burke, and S. R. White, Physical Chemistry Chemical Physics **14**, 8581 (2012).
[27] E. M. Stoudenmire and S. R. White, Physical review letters **119**, 046401 (2017).
[28] M. Dolfi, B. Bauer, M. Troyer, and Z. Ristivojevic, Physical review letters **109**, 020604 (2012).
[29] N. Mardirossian, J. D. McClain, and G. K.-L. Chan, The Journal of chemical physics **148**, 044106 (2018).
[30] Z. Y. Xie, J. Chen, J. F. Yu, X. Kong, B. Normand, and T. Xiang, Phys. Rev. X **4**, 011025 (2014).
[31] P. Corboz and F. Mila, Phys. Rev. Lett. **112**, 147203 (2014).
[32] T. Picot and D. Poilblanc, Phys. Rev. B **91**, 064415 (2015).
[33] T. Picot, M. Ziegler, R. Orús, and D. Poilblanc, Phys. Rev. B **93**, 060407 (2016).
[34] B.-X. Zheng, C.-M. Chung, P. Corboz, G. Ehlers, M.-P. Qin, R. M. Noack, H. Shi, S. R. White, S. Zhang, and G. K.-L. Chan, Science **358**, 1155 (2017).
[35] G. Fano, F. Ortolani, and L. Ziosi, The Journal of chemical physics **108**, 9246 (1998).
[36] G. K.-L. Chan and M. Head-Gordon, The Journal of chemical physics **116**, 4462 (2002).
[37] G. K.-L. Chan and S. Sharma, Annual review of physical chemistry **62**, 465 (2011).
[38] E. M. Stoudenmire and S. R. White, Physical review letters **119**, 046401 (2017).
[39] B. Pirvu, V. Murg, J. I. Cirac, and F. Verstraete, New Journal of Physics **12**, 025012 (2010).
[40] F. Fröwis, V. Nebendahl, and W. Dür, Physical Review A **81**, 062337 (2010).
[41] G. M. Crosswhite and D. Bacon, Physical Review A **78**, 012356 (2008).
[42] G. M. Crosswhite, A. C. Doherty, and G. Vidal, Physical Review B **78**, 035116 (2008).
[43] H. H. Zhao, Z. Y. Xie, Q. N. Chen, Z. C. Wei, J. W. Cai, and T. Xiang, Physical Review B **81**, 174411 (2010).
[44] R. J. Baxter, *Exactly solved models in statistical mechanics* (Academic Press, 1982) Chap. 2,7.
[45] P. Corboz, R. Orús, B. Bauer, and G. Vidal, Physical Review B **81**, 165104 (2010).
[46] J. Jordan, R. Orús, G. Vidal, F. Verstraete, and J. I. Cirac, Physical review letters **101**, 250602 (2008).
[47] D. Braess and W. Hackbusch, IMA journal of numerical analysis **25**, 685 (2005).
[48] Z. Y. Xie, H. J. Liao, R. Z. Huang, H. D. Xie, J. Chen, Z. Y. Liu, and T. Xiang, Physical Review B **96**, 045128 (2017).
[49] L. Vanderstraeten, J. Haegeman, P. Corboz, and F. Verstraete, Physical Review B **94**, 155123 (2016).
[50] P. Corboz, Physical Review B **94**, 035133 (2016).

APPENDIX A: FINITE STATE MACHINE RULES

The finite state machine picture of a PEPO views each tensor as a node in a graph, and each virtual bond of dimension D as a directed edge in that graph that can pass D different signals (or has D different possible states). Note that the following presentation of these ideas heavily follows in the spirit of Ref. [40].

Full 2D FSM. — By convention we have chosen our directed edges to point up and right so that, for a given tensor at position k, its U and R indices pass outgoing signals while its D and L indices receive incoming signals. For special combinations of incoming and outgoing signals for a tensor at position k, the corresponding tensor entry is a non-zero local operator $O^{[k]}_{n_k n'_k}$ (which may be the identity operator). These special index values are precisely the state machine rules that construct the corresponding desired state machine. When the four virtual index values do not match any of these desired rules, the value of $O^{[k]}_{n_k n'_k}$ is the zero operator $\hat{\mathbf{0}}$, meaning such a configuration of the state machine (and therefore such a configuration of the local operators) is disallowed. The complete list of rules that define the full 2D FSM PEPO which generates all pairwise interactions $\sum_{i<j} \hat{A}_i \hat{B}_j$ with bond dimension $D = 4$ is given in Table I.

Each index value corresponds to a different signal, which is used to pass a different message. "0" is the default signal, which generally means that nothing interesting is happening along that signal path. "1" is the signal that tells nearby tensors that they should not "turn on" their physical operator $O^{[k]}_{n_k n'_k}$, but instead should just return the identity operator. This is used when another tensor along a certain signal path has turned on its physical operator and does not want an interaction to be generated along the signal path on which it just sent a "1" message. "2" is the signal that is passed along the "typical" interaction path between the physical operator at site i and the physical operator at site j. A typical interaction path is one in which a signal traveling from site i to site j must only propagate upward and to the right (along the allowed directions of the directed edges). The signal "3" is reserved for the cases in which the signal traveling from site i to site j must travel to the left. In order to generate all pairs of sites, one must either have signals that travel up and to the left or down and to the right (violating one of the directed edge directions), but the case of down and to the left can be avoided due to the fact that we are generating all pairs of interactions only once (hence $i < j$ in the summations). By convention, we have chosen this pathological case to be described by a signal that travels up and to the left. Since a signal cannot travel against the direction of a directed edge, this case is resolved by having the operator at site j (the operator at the "end" of the signal) send a "3" signal to the right, which then meets with a "2" signal that was sent upwards from site i, generating an interaction along a "non-typical" path. These cases are illustrated diagrammatically in Fig. 5.

Rule number	Index values (L_k, U_k, D_k, R_k)	$O^{[k]}_{n_k n'_k}$
1	(0,0,0,0)	$\hat{I}_k$
2	(0,2,2,0)	$\hat{I}_k$
3	(2,1,0,2)	$\hat{I}_k$
4	(0,1,1,0)	$\hat{I}_k$
5	(1,1,0,1)	$\hat{I}_k$
6	(0,2,0,0)	$\hat{A}_k$
7	(0,1,0,2)	$\hat{A}_k$
8	(0,1,2,2)	$\hat{I}_k$
9	(0,1,2,1)	$\hat{B}_k$
10	(2,1,0,1)	$\hat{B}_k$
11	(3,1,0,3)	$\hat{I}_k$
12	(3,1,2,1)	$\hat{I}_k$
13	(0,1,0,3)	$\hat{B}_k$
14*	$P^{\text{top right}}_{0,0,0,0}$	$\hat{0}_k$

TABLE I. The rules for the full 2D FSM PEPO that generates all pairwise interactions $\sum_{i<j} \hat{A}_i \hat{B}_j$ with $D = 4$. All combinations of indices not listed in this table correspond to $O^{[k]}_{n_k n'_k} = \hat{0}_k$. Importantly, $\hat{A}$ and $\hat{B}$ do not have to be the same, although for the *ab initio* Hamiltonian under consideration in the main text, they are both n_k. I_k is simply the identity operator.

The rules in Table I are broken up into different groups according to what they describe. Rules 1-5 are background rules that account for the propagation of "1" and "2" signals through the FSM. Rules 6-10 give the additional rules necessary for describing a typical interaction. Rules 11-13 add the rules for non-typical interactions. Finally, Rule 14 is a special rule that only applies to the top right tensor in the network, where all signals terminate. This rule is included to disallow the state of the machine where all tensors have virtual index values $(0, 0, 0, 0)$ and a spurious 1 is added so that the final operator is $1 + \sum_{i<j} \hat{A}_i \hat{B}_j$ instead of $\sum_{i<j} \hat{A}_i \hat{B}_j$.

Snake FSM. — The snake construction for the FSM shown in Fig. 1(c) of the main text is much simpler than the full 2D FSM above because it is precisely just an MPO with a few extra dummy legs at each site so that the direct product with the Ising tensors can be performed. As discussed briefly in the main text, the operator-valued local matrices for an MPO that encodes the interactions $\sum_{i<j} \hat{A}_i \hat{B}_j$ are given by,

$$M^{[k]} = \begin{bmatrix} \hat{I}_k & \hat{A}_k & \hat{0}_k \\ \hat{0}_k & \hat{I}_k & \hat{B}_k \\ \hat{0}_k & \hat{0}_k & \hat{I}_k \end{bmatrix}. \tag{6}$$

Since this snake imposes an explicit ordering of all the sites on the 2D square lattice, it very naturally lends itself to the inclusion of fermionic statistics at the operator level via Jordan-Wigner strings. If the operators $\hat{A}_i$ and $\hat{B}_j$ are *spinless* fermionic creation or annihilation opera-

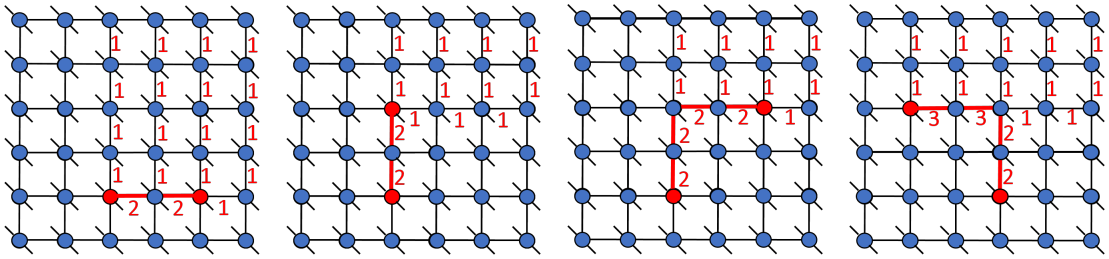

(a) (b) (c) (d)

FIG. 5. The four cases of rules needed to build the PEPO that encodes all the pairwise terms in $\sum_{i<j} \hat{A}_i \hat{B}_j$ for arbitrary operators $\hat{A}$ and $\hat{B}$. All virtual bonds are labeled with their index value, except those that are indexed 0 which are left unlabeled. The red path denotes the path of the signal from $\hat{A}_i$ to $\hat{B}_j$, which are signified by the two red tensors. Note that all the blue sites will be $\hat{I}$ in these cases.

tors (and $i < j$), then we have,

$$M^{[k]} = \begin{bmatrix} \hat{I}_k & \hat{a}_k(1-2\hat{n}_k) & \hat{0}_k \\ \hat{0}_k & 1-2\hat{n}_k & \hat{b}_k \\ \hat{0}_k & \hat{0}_k & \hat{I}_k \end{bmatrix}, \tag{7}$$

where $\hat{a}_k$ and $\hat{b}_k$ are the hard-core bosonic creation/annihilation operators and $1-2\hat{n}_k$ encodes the fermionic statistics. For *spinful* fermionic operators we have to distinguish between spin up and spin down cases. For terms like $\hat{A}_{i\uparrow}\hat{B}_{j\uparrow}$ we have ,

$$M^{[k]}_{\uparrow\uparrow} = \begin{bmatrix} \hat{I}_k & \hat{a}_k(-1)^{\hat{n}_k} & \hat{0}_k \\ \hat{0}_k & (-1)^{\hat{n}_k} & \hat{b}_k \\ \hat{0}_k & \hat{0}_k & \hat{I}_k \end{bmatrix}, \tag{8}$$

and for terms like $\hat{A}_{i\downarrow}\hat{B}_{j\downarrow}$,

$$M^{[k]}_{\downarrow\downarrow} = \begin{bmatrix} \hat{I}_k & \hat{a}_k & \hat{0}_k \\ \hat{0}_k & (-1)^{\hat{n}_k} & (-1)^{\hat{n}_k}\hat{b}_k \\ \hat{0}_k & \hat{0}_k & \hat{I}_k \end{bmatrix}. \tag{9}$$

Here $1-2\hat{n}_k$ changes to $(-1)^{\hat{n}_k}$ because we need to account for the possibility of double occupancy at a given site k, and this is also why we distinguish between the spin up and spin down cases.

APPENDIX B: Fitting methodology

There are many possible ways to fit a given long-range potential with the correlation functions of an auxiliary lattice. In this work, we first computed the Ising model correlation functions at 60 different temperatures. To choose these temperatures, we first note that away from the critical temperature of the model (T_c), the correlation functions behave according to $\sim e^{r/\xi}$, where

$$\xi \propto \left(\frac{T-T_c}{T_c}\right)^{-1}, \tag{10}$$

is the correlation length. Thus, a geometric series in $(T-T_c)/T_c$ was used to select the temperatures, starting from $T_1 = T_c + \delta$ and ending at $T_{60} = 50J/k_B$, where we chose $\delta = 5 \cdot 10^{-4}$.

With all of this data, a large "basis matrix" $\mathbf{A}$ can be formed in which each column is a correlation function at a different temperature β. We then solve the linear regression problem $\mathbf{A}\vec{c} + \vec{\epsilon} = 1/\vec{r}$, where $\vec{c}$ contains the fitting coefficients and $\vec{\epsilon}$ is the fitting error. In order to improve conditioning, a rank-revealing QR decomposition is performed on $\mathbf{A}$ to give a best guess at the N_t most relevant basis functions (temperatures). This allows for a new, smaller matrix $\tilde{\mathbf{A}}$ with only N_t columns to be formed, for which the linear regression problem is solved by weighted least-squares. Results of this fitting procedure can be seen in Figs. 2 and 6.

APPENDIX C: COMPUTATIONAL COST

In the main text we claimed that the leading computational cost for evaluating finite PEPS expectation values using the full 2D FSM CF-PEPO is

$$N_t[O(A\chi^3 D_O^3) + O(AN_f\chi^3 D_O'^2 D_O) + O(AN_f^2\chi^3 D_O'^3) + O(A\chi^3 D_S^3) + O(AN_f\chi^3 D_O'^2 D_S)].$$

Similarly, the leading cost of using the snake CF-PEPO was reported to be,

$$N_t[O(A\chi^3 D_O'^2 D_O) + O(AN_f\chi^3 D_O'^2 D_O) + O(AN_f^2\chi^3 D_O'^3) + O(A\chi^3 D_S^3) + O(AN_f\chi^3 D_O'^2 D_S)],$$

where in both cases $\chi \sim D_S^2 D_O$, D_O is the large PEPO bond dimension, $D_O' = 2$ is the Ising model bond dimension, and D_S is the PEPS bond dimension.

In the contraction scheme proposed in [48], the fundamental operation is to contract a boundary MPS of bond dimension χ with a row of tensors corresponding to either the PEPO layer or the PEPS layer, and then to perform a subsequent truncation of the boundary bond dimension

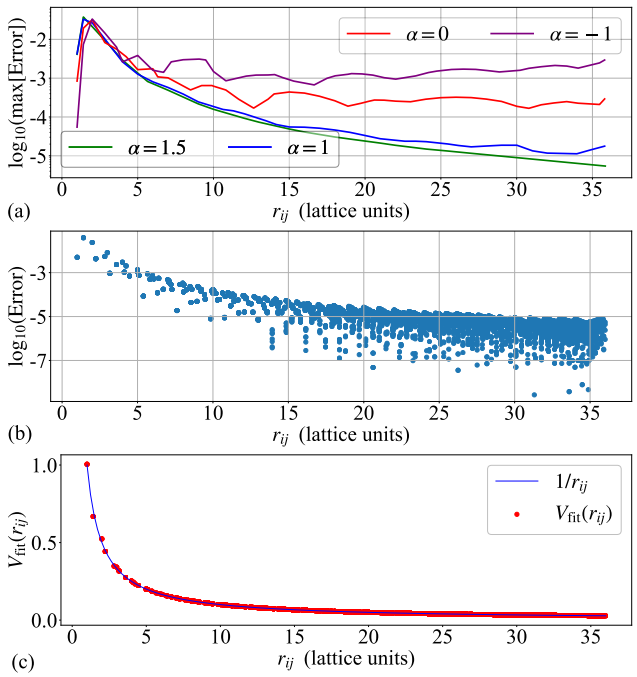

FIG. 6. (a) The upper envelope of $|V_{\rm fit}(r_{ij}) - 1/r_{ij}|$ for different least squares weight functions r_{ij}^{α} with $N_t = 12$, $L = 199$, and $r_{ij} = R_{ij}$. (b) All the errors $|V_{\rm fit}(r_{ij}) - 1/r_{ij}|$ at each r_{ij} for the $N_t = 12$, $\alpha = 1.5$, $L = 199$, $r_{ij} = R_{ij}$ fit. Note that most of the errors for a given r_{ij} are significantly smaller than the upper envelope that was shown in Fig. 2a. (c) The lattice discretized $V_{\rm fit}(r_{ij})$ compared to the continuous Coulomb potential for the $N_t = 12$, $\alpha = 1.5$, $L = 199$, $r_{ij} = R_{ij}$ fit. Note that at small values of r_{ij} the values of $V_{\rm fit}$ visibly deviate from the exact solution, while as r_{ij} grows the agreement gets significantly better.

back to χ. The main contractions which occur during this process are shown in the top row of Figure 7. The primary modification of the scheme in [48] is to account for the fact that the PEPO has two kinds of sites (fictitious and physical) which have different bond dimensions. For the full 2D FSM CF-PEPO, (a) shows the contraction of the boundary MPS with a physical site tensor in the PEPO; (b) shows the contraction of the boundary MPS with a fictitious site tensor that falls in the same row as physical site PEPO tensors; (c) shows the contraction of the boundary MPS with a fictitious site tensor that does not fall in the same row or column as the physical tensors. Diagrams nearly identical to (a) and (c) also occur when contracting the boundary MPS into the PEPS layer, with the only difference being that $D_O \to D_S$.

The dominant cost arises from the SVDs that must be performed after contraction to reduce the new composite bond dimension back to χ. The bottom row of Figure 7 shows the objects which we need to perform SVDs on, corresponding to the object that was formed by performing the contraction right above it in the Figure. The reason why the objects on the bottom row appear asymmetric along the horizontal bonds is due to the sweeping

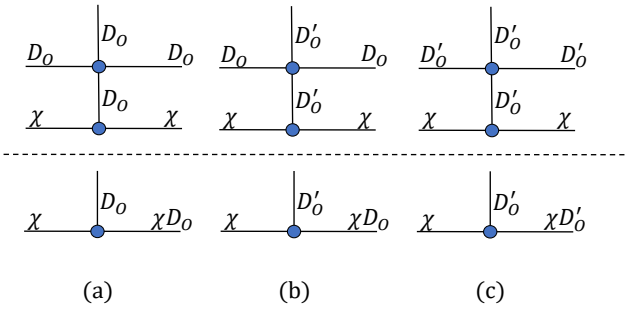

FIG. 7. Operations which occur during the evaluation of expectation values using the optimized contraction scheme. The top row shows contraction of the boundary MPS into the next row of the grid. The bottom row shows the corresponding object on which an SVD must be performed. (a) operations on physical sites of the PEPS, and also on physical sites of the full 2D FSM CF-PEPO. (b) operations on physical sites of the snake CF-PEPO, and also the operations on all fictitious or identity tensors which lie in the same row as the physical PEPO or PEPS tensors. (c) operations on PEPO fictitious sites which do not lie in the row or column of any physical sites.

nature of the SVDs, which here was assumed to sweep from left to right.

The cost of performing SVDs on these objects is as follows: $(a)_{\rm PEPO} = O(\chi^3 D_O^3)$, $(a)_{\rm PEPS} = O(\chi^3 D_S^3)$, $(b)_{PEPO} = O(\chi^3 D_O^{'2} D_O)$, $(b)_{PEPS} = O(\chi^3 D_O^{'2} D_S)$, $(c) = O(\chi^3 D_O^{'3})$, where the subscript denotes whether the boundary MPS was first contracted into the PEPS or PEPO layer.

The operations of type (a) need to be performed only $O(A)$ times, while the operations of type (b) need to be performed $O(AN_f)$ times, and the operations of type (c) need to be performed $O(AN_f^2)$ times. Thus, the total leading cost of evaluating an expectation value using the full 2D FSM CF-PEPO is

$$N_t[O(A\chi^3 D_O^3) + O(AN_f\chi^3 D_O^{'2} D_O) + O(AN_f^2\chi^3 D_O^{'3}) + O(A\chi^3 D_S^3) + O(AN_f\chi^3 D_O^{'2} D_S)].$$

To obtain the result for the snake CF-PEPO, one repeats the above analysis. The only difference is that no operations of type (a) appear for the PEPO. Instead, the PEPO physical site operations have diagrams like type (b). Thus, the first two terms of the cost of the snake PEPO look identical, except that one occurs only $O(A)$ times while the other occurs $O(AN_f)$ times.